Colorado Ultraviolet Transit Experiment Near-ultraviolet Transmission Spectroscopy of the Ultrahot Jupiter KELT-9b

Egan, A.; France, K.; Sreejith, A.G.; Fossati, L.; Koskinen, T.; Fleming, B.; Nell, N.; Suresh, A.; Cauley, P.W.; Desert, J.-M.; Petit, P.; Vidotto, A.A.

DOI
10.3847/1538-3881/ad61e5

Publication date
2024

Document Version
Final published version

Published in
Astrophysical Journal

The Astronomical Journal, 168:108 (9pp), 2024 September https://doi.org/10.3847/1538-3881/ad61e5

Colorado Ultraviolet Transit Experiment Near-ultraviolet Transmission Spectroscopy of the Ultrahot Jupiter KELT-9b

Arika Egan[1,2], Kevin France[1], Aickara Gopinathan Sreejith[1,3], Luca Fossati[3], Tommi Koskinen[4], Brian Fleming[5], Nicholas Nell[5], Ambily Suresh[1], P. Wilson Cauley[1], Jean-Michel Desert[6], Pascal Petit[7], and Aline A. Vidotto[8]
[1] Laboratory for Atmospheric and Space Physics, University of Colorado Boulder, 1234 Innovation Drive, Boulder, CO 80303, USA
[2] Applied Physics Laboratory, Johns Hopkins University, 11101 Johns Hopkins Road, Laurel, MD 20723, USA
[3] Space Research Institute, Austrian Academy of Sciences, Schmiedlstrasse 6, A-8042, Graz, Austria
[4] Lunar and Planetary Laboratory, University of Arizona, Tucson, AZ 85721, USA
[5] Laboratory for Atmospheric and Space Physics, University of Colorado Boulder, Boulder, CO 80303, USA
[6] Anton Pannekoek Institute of Astronomy, University of Amsterdam, Amsterdam, The Netherlands
[7] Institut de Recherche en Astrophysique et Planétologie, Université de Toulouse, CNRS, CNES, 14 avenue Edouard Belin, F-31400 Toulouse, France
[8] Leiden Observatory, Leiden University, P.O. Box 9513, 2300 RA, Leiden, The Netherlands
Received 2024 April 1; revised 2024 June 27; accepted 2024 July 2; published 2024 August 6

Abstract

We present new near-ultraviolet (NUV, $\lambda = 2479$–3306 Å) transmission spectroscopy of KELT-9b, the hottest known exoplanet, obtained with the Colorado Ultraviolet Transit Experiment CubeSat. Two transits were observed on 2022 September 28th and September 29th, referred to as Visits 1 and 2 respectively. Using a combined transit and systematics model for each visit, the best-fit broadband NUV light curves are $R_p/R_\star = 0.136^{+0.0125}_{-0.0146}$ for Visit 1 and $R_p/R_\star = 0.111^{+0.0162}_{-0.0190}$ for Visit 2, appearing an average of 1.54× larger in the NUV than at optical wavelengths. While the systematics between the two visits vary considerably, the two broadband NUV light curves are consistent with each other. A transmission spectrum with 25 Å bins suggests a general trend of excess absorption in the NUV, consistent with expectations for ultrahot Jupiters. Although we see an extended atmosphere in the NUV, the reduced data lack the sensitivity to probe individual spectral lines.

Unified Astronomy Thesaurus concepts: Exoplanet atmospheres (487); Ultraviolet spectroscopy (2284); Transmission spectroscopy (2133); Hot Jupiters (753); Exoplanets (498)

1. Introduction

KELT-9b is the hottest exoplanet discovered to date with an equilibrium temperature $T_{eq} \simeq 3921$ K (Borsa et al. 2019). The planet has $R_p = 1.783 \pm 0.009\, R_{Jup.}$, mass $M_p = 2.44 \pm 0.70\, M_{Jup.}$ (Hoeijmakers et al. 2019), and orbits an A0 star with $T_{eff} = 9495 \pm 104$ K (Kama et al. 2023) at a distance $a = 0.0336$ au (Kama et al. 2023) with a period $P = 1.4811$ days (Ivshina & Winn 2022), an environment that prevents aerosol formation on the planet's day side (Lothringer et al. 2018; Kitzmann et al. 2018), and possibly drives an escaping outflow. Both Hα (Yan & Henning 2018; Cauley et al. 2019) and Hβ (Cauley et al. 2019) were detected to be optically thick out to $\sim$1.61 R_p. Several metals have also been detected in the planet's atmosphere (out to 1.10 R_p and between 10^{-3} and 10^{-6} bar) with ground-based high-resolution transmission spectroscopy, including Fe I, Fe II, Ti II, Mg I, Na I, Cr I, Sc II, and Ca II (Hoeijmakers et al. 2018, 2019; Cauley et al. 2019; Yan et al. 2019; Turner et al. 2020; Bello-Arufe et al. 2022; Borsato et al. 2023a; Borsato et al. 2023b; Lowson et al. 2023). The O I triplet at 7774 Å was measured by Borsa et al. (2021), and most recently, Borsato et al. (2023b) reported new detections of Ni I, Sr I, Tb II, V I, and Ba II.

These ground-based detections have provided important constraints on the abundances, temperature–pressure profile, and overall structure of the atmosphere. Both H-Balmer lines and metal lines are best fit with model atmospheres that include nonlocal thermodynamic effects (NLTE; García Muñoz & Schneider 2019; Turner et al. 2020; Borsa et al. 2021). Compared with LTE models, the NLTE models predict upper atmospheric temperatures on the order of 8000 K (Turner et al. 2020; Borsa et al. 2021; Fossati et al. 2021).

Quantities of the upper atmosphere, like abundances and mass-loss estimates, have been made using optical absorption features, but these observations are unable to directly probe the upper atmosphere (Fossati et al. 2021). For example, the Hα and Ca II detections from Turner et al. (2020) were found at effective altitudes between 1.2 and 1.44 R_p. The O I triplet in Borsa et al. (2021) was measured with an effective altitude of 1.17 R_p. KELT-9b is believed to have an escaping atmosphere, but detections of such have not been conclusively made, as the planet's Roche lobe is at 2.017 R_p (Section 4).

Ultraviolet transmission spectroscopy can provide a unique complement to atmospheric characterization studies. The near-ultraviolet (NUV) bandpass between $\sim$1800 and 3500 Å contains hundreds of strong and abundant metal lines like Fe and Mg (Fossati et al. 2010; Haswell et al. 2012) that have been observed escaping in several planetary atmospheres (Sing et al. 2019; Sreejith et al. 2023). Observations of high-altitude and escaping metal lines can constrain the energy balance and ionization states of the upper atmospheric layers (Cubillos et al. 2020, 2024). For example, Mg was determined to be an important coolant in the upper atmospheres of HD189733b (Huang et al. 2017) and KELT-20b (Fossati et al. 2023), and Fe was found to be strongly tied to atmospheric heating (Fossati et al. 2021). In addition, NUV observations have been used to assess the presence of scattering hazes (Wakeford et al. 2020; Lothringer et al. 2022; Gressier et al. 2023).

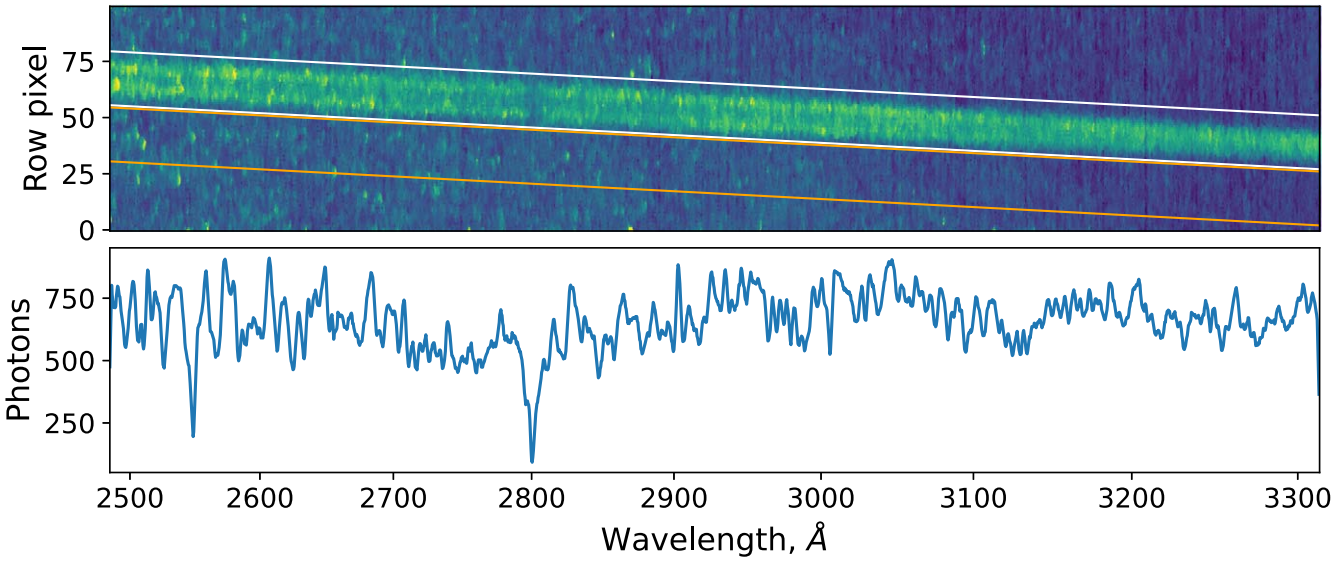

Figure 1. Top: a 2D CUTE CCD image of a single 5 minutes exposure. The image is bias-subtracted and corrected for bad pixels and cosmic rays. The spectral extraction region is outlined in white, and the background region is outlined in orange. Bottom: the summed 1D spectrum after background subtraction, smoothed with a Gaussian filter for display purposes.

Table 1
CUTE KELT-9b Observations

Visit #	Visit Start (2022 UTC)	Midtransit Time (2022 UTC)	Visit End (2022 UTC)	Total Orbits	Total Frames	Valid Frames[a]
1	Sep 27-14:54	Sep 28-01:36	Sep 28-12:02	13	46	44
2	Sep 29-02:09	Sep 29-13:09	Sep 30-00:47	15	57	54

Note.
[a] A valid frame has spacecraft pointing jitter $<10''$ rms.

Here we present new NUV observations of KELT-9b obtained with the Colorado Ultraviolet Transit Experiment (CUTE), a CubeSat mission dedicated to exploring the upper atmospheres of highly irradiated ultrahot Jupiters (France et al. 2023). We first provide an overview of the CUTE CubeSat and describe the KELT-9b observations in Section 2. Section 3 describes the data reduction and general light-curve modeling. Broadband NUV light curves with 100 Å and 25 Å transmission spectra are presented in Section 4, and a summary is provided in Section 5.

2. Observatory and Observations

2.1. CUTE Instrument Description

The CUTE instrument is an NUV spectrograph operating between 2479 and 3306 Å with $R \sim 750$ and an average dispersion of 0.404 Å pixel^{-1}. CUTE operates in low-Earth orbit with a period of about 95 minutes and an inclination of ∼98°. Like transit observations obtained with the Hubble Space Telescope (HST), CUTE time-series observations exhibit gaps in coverage due to Earth occultations. The spectrum is recorded on a passively cooled back-illuminated CCD with 515 × 2048 (spatial × spectral) active pixels (Nell et al. 2021). The CCD experiences temperatures between −5°C and −12°C over the course of an orbit, resulting in a temperature-dependent dark current that is included in our systematics modeling and removal, as described in Section 3 and Egan et al. (2023). A two-dimensional spectrum trimmed to 100 rows centered around the spectral trace, and the one-dimensional spectrum, are shown in Figure 1.

2.2. KELT-9b observations

Two successive transits of KELT-9b were observed with CUTE in 2022 on September 28th and September 29th, referred to hereafter as Visit 1 and Visit 2, respectively. Each visit was planned such that the full observation window was 5× the 3.91 hr transit duration, resulting in ≈±10.5 hr on either side of the transit center. Bias and dark frames were obtained before and after each observation window with a 0°.75 pointing offset to point the CUTE aperture at dark sky but maintain similar sky background levels. Exposures are 5 minutes each and Visit 1 consists of 13 CUTE orbits and Visit 2 consists of 15 orbits, each with four CCD exposures per orbit. While the CUTE spacecraft is in Earth's shadow for approximately half of the 95 minutes orbit, Earth and moon avoidance angles as well as time required for the spacecraft to settle into fine-pointing mode reduce the total available observing time to approximately 20–30 minutes per orbit. Occasionally, the CUTE spacecraft exhibits anomalously high pointing jitter within a given 5 minutes observation that smears the spectrum across a larger region of the detector. This reduces the per-pixel signal to noise, and integrating over more pixels results in a reduction of the overall signal-to-noise ratio of those exposures compared to a low-jitter frame, rendering them unusable in light-curve analysis. Observations with a jitter $>10''$ rms are excluded from light-curve analysis. Table 1 provides a summary of the observations analyzed herein.

3. Data Analysis

3.1. Data Reduction

The data were reduced using a modified process of the CUTE Data Reduction Pipeline (Sreejith et al. 2022). Raw stellar frames are corrected for bad pixels and cosmic rays. Bias frames are corrected for bad pixels and cosmic rays, and a master bias frame is created by taking the median of the corrected individual bias frames from each visit; this master bias frame is then subtracted from all stellar frames. The background is estimated and subtracted using the bias-subtracted frame. Bad pixels are replaced with the median of a 3×3 grid of nonbad pixels surrounding the bad pixel. Cosmic rays are identified and replaced using the L.A. Cosmic routine (van Dokkum 2001). A region is defined around the spectrum and summed to create a one-dimensional stellar + background spectrum. A background region below the spectrum of the same size as the stellar region is summed to form a background one-dimensional spectrum that is subtracted from the stellar + background spectrum to produce the final 1D stellar spectrum. The stellar and background regions are shown in the top panel of Figure 1 as surrounded by the white and orange lines respectively, and the corresponding 1D stellar spectrum is shown in the bottom panel of Figure 1. To create a broadband NUV light curve, the entire spectral bandpass is summed and plotted in time; the NUV light curves for Visits 1 and 2 are shown in Figure 2.

3.2. Light Curve and Systematics Fitting

Like other space telescopes (e.g., HST; Wakeford et al. 2016; Gressier et al. 2023) CUTE exhibits orbital- and visit-dependent systematics. As seen in the top plot of Figure 2, the systematics embedded in both visits take different forms, though a transit signal appears to be present in both. Out of transit, the uncorrected counts vary by 10.8% in Visit 1 and 8.8% in Visit 2. CUTE systematics are heavily correlated with its orbit, evident in the trend of decreasing counts as a function of CUTE orbit, a trend visible in the normalized uncorrected light curves for both Visits 1 and 2. These trends are strongly related to the temperature of the CCD, which varies approximately 6°C per orbit (Egan et al. 2023), starting at higher temperatures as CUTE enters the Earth's shadow and cools until exiting the shadow. In addition to thermal trends, CUTE's wide field of view and compact design (Fleming et al. 2018; Egan et al. 2020) subjects the focal plane to low scattered light levels that change throughout an orbit and throughout a visit. Finally, pointing jitter increases the extent of the spectral trace on the detector, reducing the observation's signal-to-noise ratio.

There are several parameters that describe CUTE's pointing that are related to the CCD temperature, scattered light levels, and exhibit covariances among each other (e.g., Figure 3 in Egan et al. 2023): Azimuth and elevation angles of the telescope with respect to (1) the Earth, (2) the Sun, and (3) the Moon; the Earth latitude and longitude over which the observation began; the CCD temperature; and the R.A., decl., and roll angles of the telescope. Several of these 12 parameters are necessary to detrend the raw light curves and isolate the astrophysical signal from the background. Individually, all of these parameters are correlated with the background levels by some function (e.g., linear, quadratically), as well as related to each other. Due to the covariance among the parameters, it becomes challenging to include all of them, or select a subset

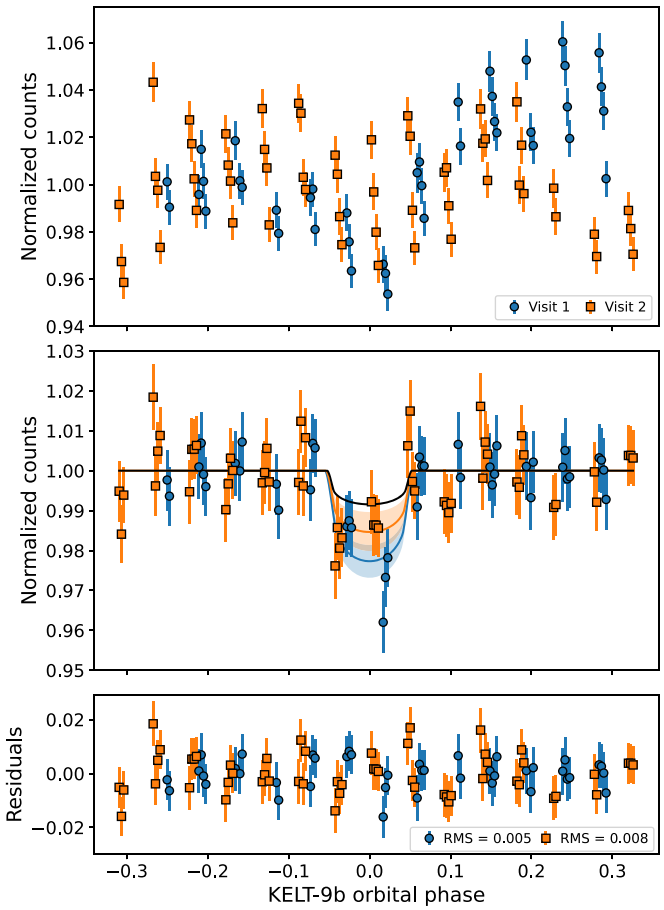

Figure 2. CUTE raw, broadband NUV light-curve best fits, and residuals for KELT-9b Visit 1 (blue circles) and Visit 2 (orange squares). Each data point represents a 5 minutes exposure. Top: the uncorrected counts normalized to the median of the first three CUTE orbits, which are out of transit. Middle: the normalized counts with the best-fit instrument systematics model removed, 1σ error bars and each visit's light-curve model in their respective colors. The 1σ R_p/R_* regions are transparently shown in each visit's respective colors. The black line transit is the optical transit light curve from Wong et al. (2020). Bottom: the residuals with 1σ error bars. The two light curves are shown on the same plot to emphasize the difference in systematics across each visit.

that best describes the systematics. To include as many parameters as possible in the detrending analysis, we utilized principal component analysis (PCA) using the 12 parameters listed above.

PCA transforms a set of correlated or potentially correlated variables into an orthogonal set of uncorrelated variables, each called a principal component. It does so by scaling each variable to unit variance, calculating the covariance matrix of the unit-scaled set, and then decomposes the covariance matrix into eigenvectors, or the principal components (PCs). Each PC is then responsible for some level of variation in the whole data set. We used the python `scikit-learn` package (Pedregosa et al. 2011) to carry out the PCA, and the PCs for visits 1 and 2 are shown in Figure 3, plotted against the transit phase.

From Figure 3, it is evident how different the CUTE spacecraft states are between Visits 1 and 2. For both visits, PC 0 is likely heavily influenced by the detector temperature, as each spacecraft orbit, which typically contains 4 exposures (though there are a few in each visit with only 3 or 2 exposures) begins with a higher temperature as the spacecraft enters the Earth's shadow, with successively lower temperatures as the spacecraft cools within the shadow. Hence, the appearance of 4

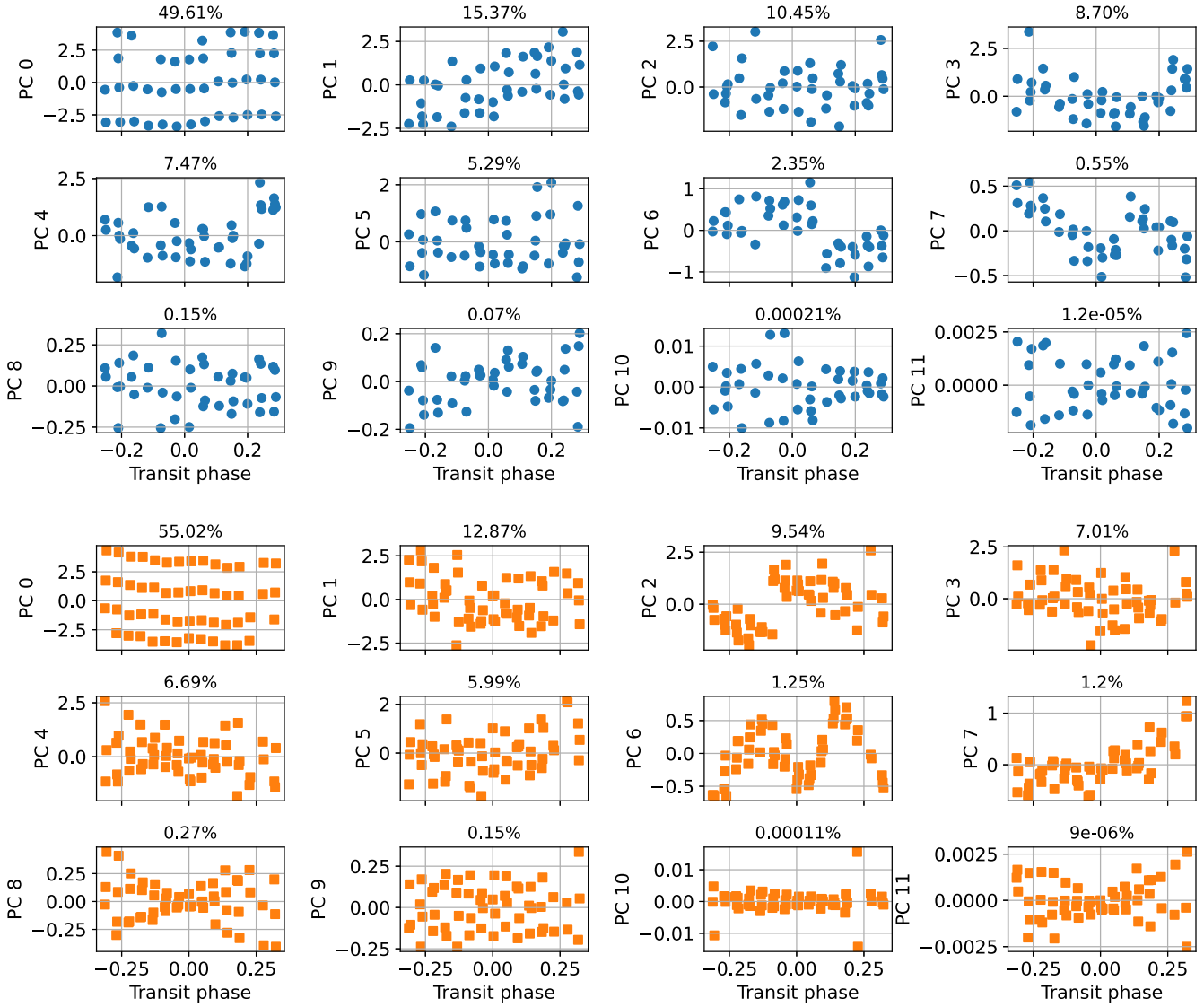

Figure 3. Top: the principal components for Visit 1. Bottom: the principal components for Visit 2, both plotted against the KELT-9b orbital phase. Each PC's variance is shown in the respective plot title.

distinct rows in PC 0 for both Visits 1 and 2 is due to exposures being taken at similar locations in a given orbit. There are PCs that exhibit dips near the midtransit time, which may have otherwise been mistaken as a transit signal. For example a dip is very evident in PC 6 for Visit 2, and more subtly in PC 0 for Visit 1. We emphasize that no CUTE observations were used in the PCA for either visit, only CCD temperature and spacecraft orientation values.

We model the total flux in an exposure, f, as the sum of a stellar flux offset, F_0, a transit light-curve model in both time t and transit parameters Θ, $T(t, \Theta)$, and a systematics model consisting of the sum of first-order polynomials for the 12 PCs, additional first-order polynomials for the jitter components, j, along the x, y, and z spacecraft axes:

$$f = F_0 + T(t, \Theta) + \sum_{i=1}^{i\leqslant 12} a_i \mathrm{PC}_i + \sum_{i=x}^{z} b_i j_i, \qquad (1)$$

where a_i are the coefficients for the PCs and b_i are the coefficients for the jitter term j. As shown in Figure 3, each PC does not contribute equally to the total variance in the PC data set, but rather each subsequent PC has a small total variance contribution. PC 0 has the largest variance out of all the PCs, with 49.61% for Visit 1 and 55.02% for Visit 2.

The use of PCA with the chosen parameters limits us to a first-order polynomial. The raw CUTE counts correlate linearly with the CCD temperature, and since PCA produces a set of orthogonal components, one of which is strongly linear with CUTE data, all other PCs are limited to a first-order polynomials as well.

We use `batman` (Kreidberg 2015) as $T(t, \Theta)$ and let only the planetary to stellar radius ratio, $R_p/R_\star$ float as a free parameter. The planet's midtransit time, semimajor axis, eccentricity, longitude of periapsis, and orbital inclination were fixed to nominal values listed in Table 2. The CUTE data does not have enough coverage during ingress and egress to fit for limb-darkening coefficients, so we instead used `limb-darkening` package (Espinoza & Jordán 2015) to calculate quadratic-law limb-darkening coefficients using stellar parameters from Table 2. The `lmfit` python package was used to carry out an MCMC fit to each model.[9]

[9] We provide details of this process in Appendix.

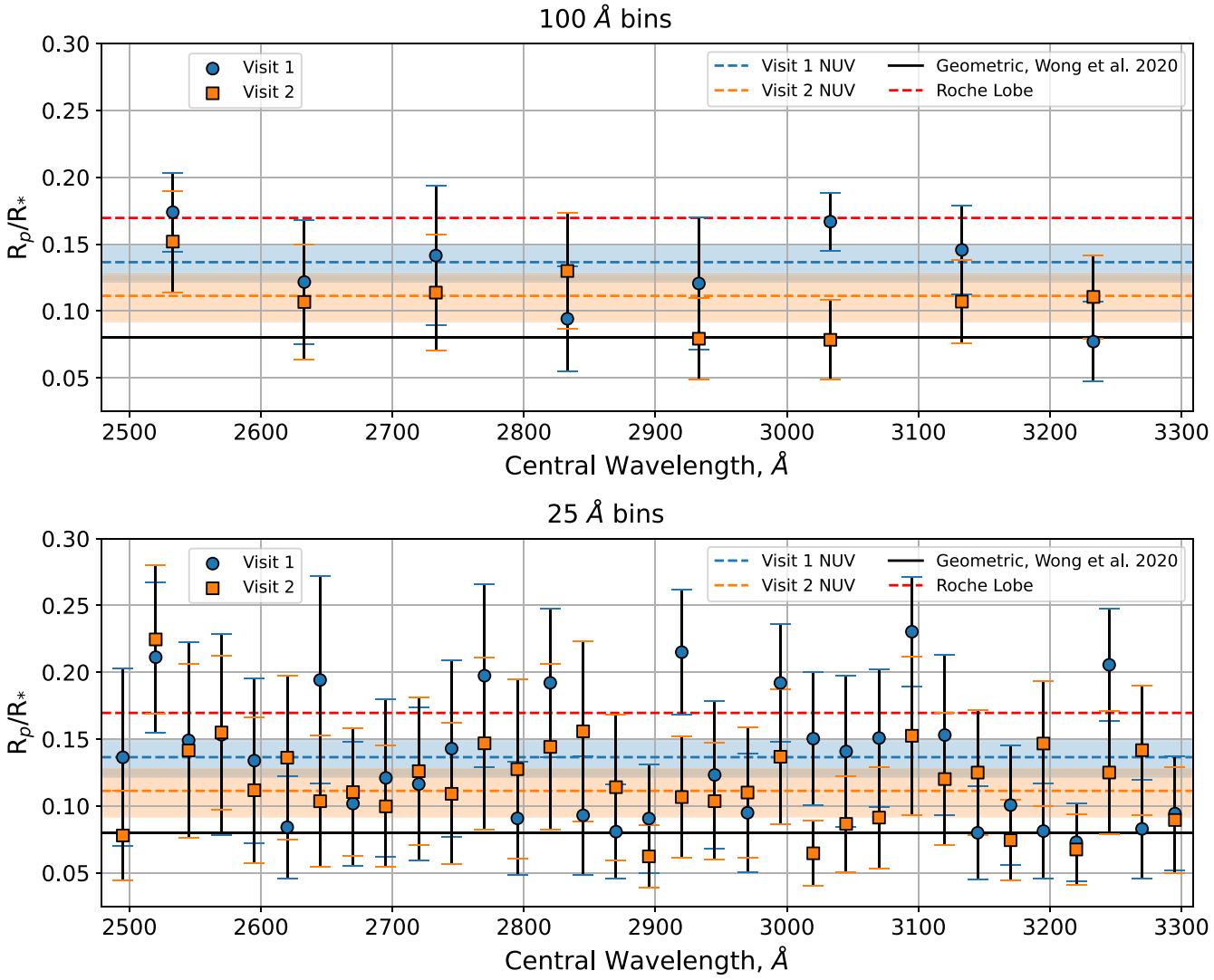

Figure 4. Top: transmission spectrum for Visit 1 and Visit 2 with 100 Å wide bins, corresponding to $R \sim 28$. Bottom: transmission spectrum for Visit 1 and Visit 2 with 25 Å wide bins, corresponding to $R \sim 112$. On both plots, the Roche Lobe radius is shown as the red dashed line, and the visible light $R_p/R_\star$ from Wong et al. (2020) is shown as the black solid line.

Table 2
KELT-9 System Parameters, Θ

Parameter	Unit	Symbol	Value	Source
Stellar effective temperature	K	$T_{\rm eff}$	10170	Gaudi et al. (2017)
Stellar mass	$M_\odot$	$M_\star$	1.978 ± 0.023	Hoeijmakers et al. (2019)
Stellar radius	$R_\odot$	$R_\star$	2.178 ± 0.011	Hoeijmakers et al. (2019)
Stellar surface gravity	cgs	log(g)	4.093	Gaudi et al. (2017)
Semimajor axis	au	a	0.03368	Borsa et al. (2019)
Planet mass	$M_{\rm Jup.}$	$M_{\rm p}$	2.44 ± 0.70	Hoeijmakers et al. (2019)
Planet radius	$R_{\rm Jup.}$	$R_{\rm p}$	1.783 ± 0.009	Hoeijmakers et al. (2019)
Orbital period	Days	P	1.48111871	Ivshina & Winn (2022)
Transit center time	Julian Date	$T_{\rm c}$	2457095.68572	Ivshina & Winn (2022)
Inclination	degree	i	86.79	Gaudi et al. (2017)
Eccentricity	degree	ε	0	Jones et al. (2022)
Argument of periastron	degree	ϖ	90	Jones et al. (2022)

We first ran Equation (1) without including jitter to identify which PCs were necessary to produce the best fit. To identify a starting point for which PCs should be included in the model, we use the KELT-9b optical transit depth, ∼0.8%, to define the minimum variance a PC must have to necessarily be included in the model. This requires that PCs 0–8 are included for Visit 1 and PCs 0–9 for Visit 2. We then reran the model including successive PCs until all 12 were included. As is done in

Table 3
KELT-9b Transmission Spectrum, 100 Å bin Widths

Central λ, Å	Visit 1 $R_p/R_\star$	Visit 2 $R_p/R_\star$
2533	$0.174^{+0.0246}_{-0.0294}$	$0.152^{+0.0300}_{-0.0378}$
2633	$0.122^{+0.0366}_{-0.0461}$	$0.107^{+0.0361}_{-0.0427}$
2733	$0.141^{+0.0399}_{-0.0521}$	$0.114^{+0.0362}_{-0.0433}$
2833	$0.094^{+0.0363}_{-0.0394}$	$0.130^{+0.0346}_{-0.0435}$
2933	$0.121^{+0.0410}_{-0.0493}$	$0.079^{+0.0301}_{-0.0305}$
3033	$0.167^{+0.0185}_{-0.0218}$	$0.078^{+0.0306}_{-0.0299}$
3133	$0.146^{+0.0247}_{-0.0333}$	$0.107^{+0.0249}_{-0.0311}$
3233	$0.077^{+0.0311}_{-0.0299}$	$0.111^{+0.0240}_{-0.0314}$

Table 4
KELT-9b Transmission Spectrum, 25 Å bin Widths

Central λ, Å	Visit 1 $R_p/R_\star$	Visit 2 $R_p/R_\star$
2495	$0.136^{+0.0578}_{-0.0666}$	$0.078^{+0.0440}_{-0.0335}$
2520	$0.211^{+0.0429}_{-0.0562}$	$0.225^{+0.0458}_{-0.0556}$
2545	$0.149^{+0.0702}_{-0.0732}$	$0.142^{+0.0584}_{-0.0650}$
2570	$0.153^{+0.0660}_{-0.0750}$	$0.155^{+0.0475}_{-0.0576}$
2595	$0.134^{+0.0548}_{-0.0616}$	$0.112^{+0.0624}_{-0.0545}$
2620	$0.084^{+0.0575}_{-0.0383}$	$0.136^{+0.0583}_{-0.0615}$
2645	$0.194^{+0.0572}_{-0.0775}$	$0.104^{+0.0572}_{-0.0488}$
2670	$0.102^{+0.0506}_{-0.0463}$	$0.110^{+0.0414}_{-0.0477}$
2695	$0.121^{+0.0632}_{-0.0588}$	$0.100^{+0.0475}_{-0.0454}$
2720	$0.116^{+0.0611}_{-0.0571}$	$0.126^{+0.0504}_{-0.0554}$
2745	$0.143^{+0.0545}_{-0.0660}$	$0.109^{+0.0568}_{-0.0528}$
2770	$0.197^{+0.0512}_{-0.0685}$	$0.147^{+0.0525}_{-0.0644}$
2795	$0.091^{+0.0569}_{-0.0426}$	$0.128^{+0.0638}_{-0.0671}$
2820	$0.192^{+0.0411}_{-0.0553}$	$0.144^{+0.0502}_{-0.0618}$
2845	$0.093^{+0.0508}_{-0.0442}$	$0.156^{+0.0591}_{-0.0675}$
2870	$0.081^{+0.0491}_{-0.0353}$	$0.114^{+0.0569}_{-0.0546}$
2895	$0.091^{+0.0505}_{-0.0405}$	$0.062^{+0.0355}_{-0.0231}$
2920	$0.215^{+0.0376}_{-0.0467}$	$0.107^{+0.0434}_{-0.0456}$
2945	$0.123^{+0.0466}_{-0.0550}$	$0.104^{+0.0398}_{-0.0434}$
2970	$0.095^{+0.0599}_{-0.0445}$	$0.110^{+0.0459}_{-0.0488}$
2995	$0.192^{+0.0354}_{-0.0441}$	$0.137^{+0.0390}_{-0.0503}$
3020	$0.150^{+0.0372}_{-0.0501}$	$0.065^{+0.0364}_{-0.0244}$
3045	$0.141^{+0.0446}_{-0.0566}$	$0.087^{+0.0346}_{-0.0360}$
3070	$0.151^{+0.0399}_{-0.0516}$	$0.091^{+0.0371}_{-0.0380}$
3095	$0.230^{+0.0328}_{-0.0409}$	$0.153^{+0.0461}_{-0.0593}$
3120	$0.153^{+0.0455}_{-0.0600}$	$0.120^{+0.0398}_{-0.0496}$
3145	$0.080^{+0.0471}_{-0.0350}$	$0.125^{+0.0368}_{-0.0470}$
3170	$0.101^{+0.0450}_{-0.0449}$	$0.074^{+0.0369}_{-0.0304}$
3195	$0.081^{+0.0483}_{-0.0356}$	$0.147^{+0.0364}_{-0.0470}$
3220	$0.073^{+0.0415}_{-0.0294}$	$0.067^{+0.0403}_{-0.0265}$
3245	$0.206^{+0.0337}_{-0.0422}$	$0.125^{+0.0366}_{-0.0461}$
3270	$0.083^{+0.0520}_{-0.0370}$	$0.142^{+0.0383}_{-0.0483}$
3295	$0.094^{+0.0485}_{-0.0427}$	$0.090^{+0.0473}_{-0.0396}$

Cubillos et al. (2024), Gressier et al. (2023), and Sreejith et al. (2023), the best-fit model is identified as that which minimizes the corrected Akaike information criterion for small samples, AICc, defined as

$$\mathrm{AICc} = \chi^2 + \frac{2k(k+1)}{n-k-1}, \tag{2}$$

where k is the number of free parameters and n are the number of data points. Once the best-fit model is found for the NUV broadband light curve, the same functional form is used to fit the spectral light curve. An analysis of the background levels across the spectral axis of the CCD show variation, indicating that the systematics model will vary as a function of pixel location along the spatial axis on the detector. Additionally, scattered light levels across the CCD are not flat (e.g., see Figure 8 in Egan et al. 2023). Therefore, we expect the same general trends to appear across CUTE's bandpass, but with different magnitudes that are dependent on the spatially inhomogeneous scattered light levels. This is in contrast to the assumption that systematics vary weakly with wavelength, as is commonly found in studies of HST data (e.g., Wakeford et al. 2016; Sing et al. 2019; Gressier et al. 2023).

4. Results and Discussion

We show the broadband NUV light curves for Visits 1 and 2 in Figure 2; the top plots show the uncorrected counts normalized to the first three out-of-transit orbits, the middle plot shows the best fit broadband NUV light curve atop the systematics-removed CUTE data with the error regions shaded in the respective colors, and the bottom plot shows the residuals. For both visits, the best model included the minimum number of PCs; when each additional PC was included in the model, the AICc grew by less than 1 for both visits, indicating that additional PCs do not improve the fit and are functionally the same. For both visits, the best-fit model was found when only the x-axis jitter was included. We find this reasonable as jitter along the x-axis translates into jitter along the shorter telescope axis, or along the spatial direction of the detector (i.e., vertically as shown in Figure 1).

For both visits, Figure 2 demonstrates the importance of a long out of transit baseline for constraining the out-of-transit continuum level in the presence of noisy data. Whereas CUTE was able to observe KELT-9b for approximately 22 hr for each transit, HST STIS using the MAMA detectors, the other operating instrument capable of obtaining NUV transmission spectroscopy, is typically limited to a maximum of five orbits per target, or approximately 8 hr, with rare exceptions being granted to allow up to six orbits (Medallon et al. 2023).

While the broadband raw light curves for Visits 1 and 2 vary considerably from each other, the best-fit light curves are consistent with each other. The best fit $R_p/R_\star$ for Visits 1 and 2 respectively are: $R_p/R_{\star V1} = 0.136^{+0.0125}_{-0.0146}$ with a reduced chi-squared $\chi^2_\nu = 1.0053$, and $R_p/R_{\star V2} = 0.111^{+0.0162}_{-0.0190}$ with $\chi^2_\nu = 0.9987$. Compared to the TESS red-optical $R_p/R_{\star opt} = 0.0804$ from Wong et al. (2020), KELT-9b appears an average of 1.54× larger in the NUV. This means that the NUV broadband transit is probing relatively low pressures in the atmosphere. The corresponding Roche lobe filling factor is larger than that observed for other hot Jupiters such as HD 209458b and HD 189733b but not as large as for the ultrahot Jupiter WASP-121b (e.g., compare Figure 4 in this paper to Figure 8 in Cubillos et al. 2024). In principle, the results for KELT-9b here appear similar to those for WASP-189b where CUTE observations indicated that the upper atmosphere of the planet is hotter and more extended than expected (Sreejith et al. 2023). The interpretation of the observations of KELT-9b, however, is complicated by the uncertainty on planet mass that allows for a range of solutions on atmospheric structure and

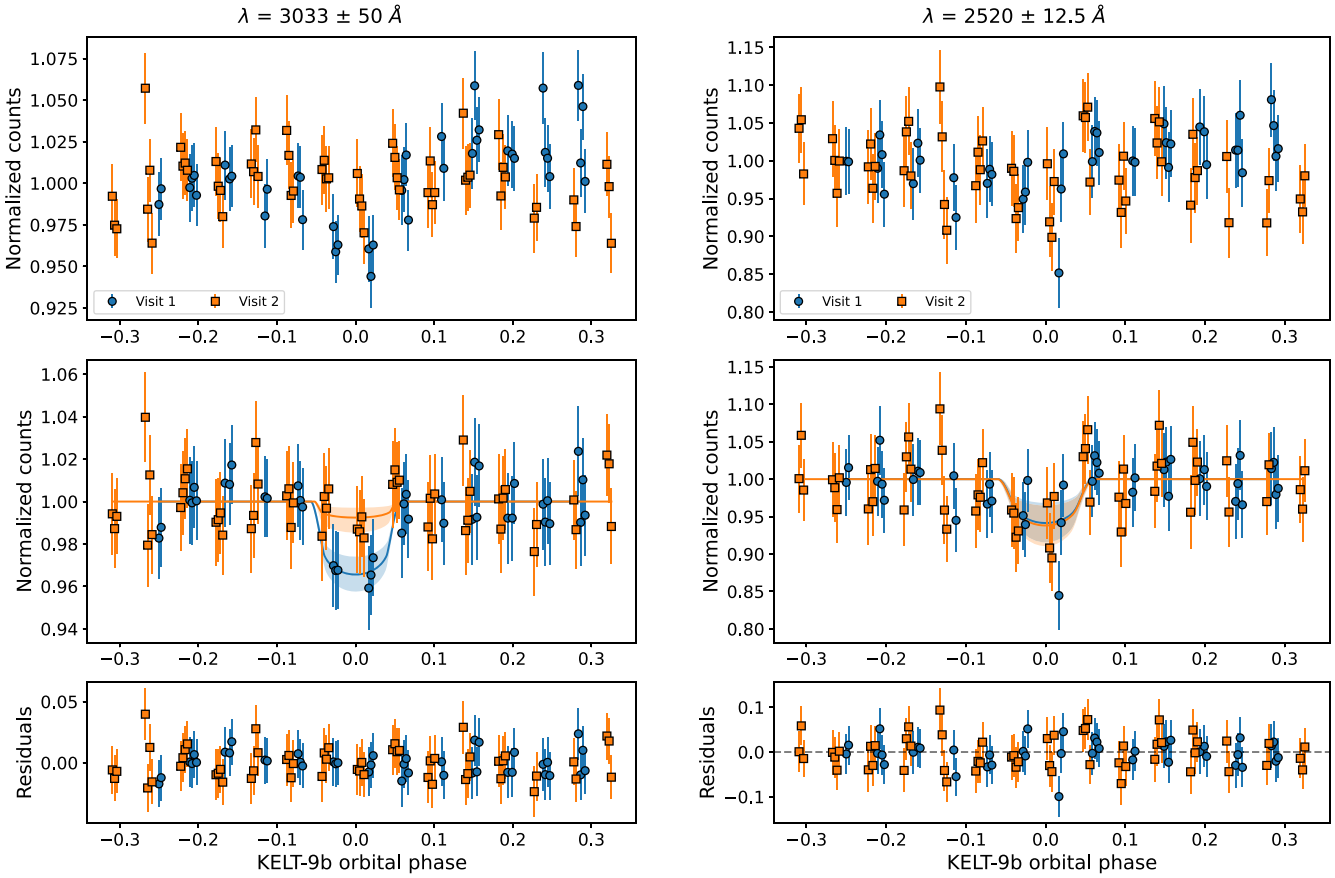

Figure 5. Left: light curves for Visits 1 and 2 for a 100 Å wide bin centered at 3033 Å. Right: light curves for Visits 1 and 2 for a 25 Å wide bin centered at 2520 Å.

mass loss (Borsa et al. 2019; Hoeijmakers et al. 2019; Lowson et al. 2023).

We attempted a joint fit between the two visits by keeping the $R_p/R_\star$ as a shared parameter and the systematics models separate for each visit. However, the joint fit produced a $R_p/R_\star$ equal to the average of the individual fits with a $\chi^2_\nu = 1.35$. We therefore keep the remaining analysis to a per-visit basis.

To further explore the light-curve differences, we produced a transmission spectrum with 100 Å and 25 Å wide bins, corresponding to $R \sim 28$ and 112 respectively, for each visit. Using the approximation from Eggleton (1983) and the values in Table 2, we calculate the Roche Lobe radius to be $R_L = 2.017\,R_p$ and include it as a visual reference. For each bin in Figure 4, we used the same fitting procedure as in Section 3. These transmission spectra are shown in Figure 4, and in Tables 3 and 4.

In the 100 Å transmission spectrum, the two visits are generally consistent with each other except at the central wavelength of 3033 Å, where Visit 1 exhibits a transit depth about 2.5σ times greater than Visit 2 and is $\geqslant 3\sigma$ larger than the optical light measurement from Wong et al. (2020). The light curves for that bin is shown in Figure 5.

A transmission spectrum with smaller bins would aid in assessing what might be responsible for the difference between the two visits at 3033 Å and to search for signs of strongly absorbing ions. Additional transit observations would be necessary to increase the required signal-to-noise ratios for finer line detection. The 25 Å spectrum, shown in the bottom half of Figure 4, indicates that Visits 1 and 2 are generally consistent with each other within their 1σ uncertainties. The shape of the 25 Å transmission spectrum is generally more noisy for Visit 1 than it is for Visit 2, which may be due to unidentified or remaining systematics.

There are a few hints of extended absorption in the CUTE NUV transmission spectrum. The 25 Å bin centered at 2520 Å shows that both visits are $>1\sigma$ above the broadband visible $R_p/R_\star$ with Visit 1 being 1.3σ greater and Visit 2 being 2.05σ greater. Three additional 25 Å bins in Visit 1 also show $>1\sigma$ above the broadband NUV $R_p/R_\star$, located at 2920 Å, 3095 Å and 3245 Å. The bin at 3095 Å lies $>1\sigma$ above the planet's Roche lobe, directly suggesting an escaping atmosphere. However, without small wavelength bins, it is challenging to discern which atomic species might be responsible for the increased absorption.

As discussed in several papers, the NUV is filled with neutral and ionized atoms that can induce extended transit depths, and KELT-9b has had a wealth of atomic detections made in optical wavelengths, motivating a search for them in the NUV where atomic transitions tend to be stronger than in the optical. For example, Fe, which has several lines present in CUTE's bandpass (e.g., Sing et al. 2019), has been detected several times with ground-based spectrographs: Cauley et al. (2019) detected nine individual lines of Fe II with the PEPSI spectrograph; both Fe I and Fe II were observed in Lowson et al. (2023) with TRES; and Fe II definitively detected in Borsato et al. (2023a) with FOCES and in Bello-Arufe et al. (2022) with FIES. We note that the spectrum of WASP-121b that shows the clearest NUV signatures of escaping metals to date (Sing et al. 2019) can be explained by Fe II lines that dominate the spectrum and the strong Mg II h&k lines (see Figure 23 in Huang et al. 2023 for a model fit). While the absorption in the

CUTE spectrum at 2520 Å coincides with Fe II lines, absorption due to Fe II at 2600 Å, which was seen in WASP-121b (Sing et al. 2019), is not present in the CUTE spectrum. At the same time, neither the model or observations of Fe II in WASP-121b show strong features at 2920 Å or 3095 Å.

The Mg II resonance lines at 2800 Å are expected to be present in KELT-9b as they have been observed in the ultrahot Jupiters WASP-12b (Fossati et al. 2010; Haswell et al. 2012), WASP-189b (Sreejith et al. 2023), and WASP-121b (Sing et al. 2019). Interestingly, there is no suggestion in the 100 Å or 25 Å transmission spectra of significantly extended absorption around 2800 Å. It is possible that residual systematics are masking the transit signal, however. In any case, the available data are unable to produce meaningfully smaller resolution transmission spectra.

5. Conclusion

Herein we presented NUV transmission spectroscopy of the ultrahot Jupiter KELT-9b obtained with the CUTE CubeSat. Two consecutive transit observations of KELT-9b, made on 2022 September 28 and 29, show differing raw light curves but consistent best-fit NUV radii. In order to maximize the number of spacecraft parameters used to detrend the data, we used principal component analysis to transform a set of correlated spacecraft parameters into a set of orthogonal parameters. From that, the two NUV broadband light curves produced consistent transit depths, with Visit 1 having $R_p/R_\star = 0.136^{+0.0125}_{-0.0146}$ and Visit 2 having $R_p/R_\star = 0.111^{+0.0162}_{-0.0190}$.

We further produced two transmission spectra, with 100 Å and 25 Å wide bins, respectively. Within the error bars, the transmission spectra are consistent between the two visits. However, the data do not have enough sensitivity to spectroscopically isolate specific atomic absorbers. The 25 Å transmission spectrum contains three bins with absorption above the Roche lobe boundary with greater than 1σ significance. However, Visit 2 does not exhibit the same signal, and in general the Visit 1 and Visit 2 25 Å transmission spectra have different shapes, perhaps suggesting that there are uncharacterized systematics remaining in the spectral light curves. It is part of our future work to explore these hints of atmospheric escape.

Despite the data quality, the broadband NUV transit depth of the low-resolution CUTE spectra show promise for the direct detection of an escaping atmosphere on KELT-9b. We are continuing to assess additional methods for removing the systematics present in the data and resolving the disagreement between Visits 1 and 2 in the higher resolution transmission spectra. Additional higher resolution spectra obtained with e.g., HST STIS will likely provide rich insight into KELT-9b's upper atmosphere.

Acknowledgments

Much of this work was funded by NASA grants NNX17AI84G and 80NSSC21K166 (PI- K. France). A.A.V. acknowledges funding from the European Research Council (ERC) under the European Union's Horizon 2020 research and innovation program (grant agreement No 817540, ASTROFLOW). A.G.S. was supported by the Schrödinger Fellowship through the Austrian Science Fund (FWF) [J 4596-N]. We are additionally grateful for the thoughtful and thorough feedback provided by the reviewer.

Facility: CUTE

Software: `batman` (Kreidberg 2015), `lmfit` Newville et al. (2015), `CONTROL` Sreejith et al. (2022), `scikit-learn` Pedregosa et al. (2011).

Appendix
Using lmfit

`lmfit` enables a modular approach to model creation and curve fitting. The `Model` class turns a given function into a model to be fit with, and several `Model` classes with different independent variables and parameters can be added together, producing a `CompositeModel` class. The `models` module has several `Model` classes built in, including a polynomial model, called `PolynomialModel` up to the 7th degree. In a `CompositeModel`, a `Model` class can only have a single independent variable even if instantiated multiple times, i.e., the user cannot instantiate `PolynomialModel(x) + PolynomialModel(y)` as they have two different independent variables. To enable the sum of polynomials in Equation (1), we utilized the open source nature of `lmfit` and added several more Polynomial models to account for all PCs and jitter terms (i.e., `PolynomialModelB`, `PolynomialModelC`, `PolynomialModelD`, etc.).

ORCID iDs

Arika Egan https://orcid.org/0000-0002-4701-8916
Kevin France https://orcid.org/0000-0002-1002-3674
Aickara Gopinathan Sreejith https://orcid.org/0000-0002-4166-4263
Luca Fossati https://orcid.org/0000-0003-4426-9530
Tommi Koskinen https://orcid.org/0000-0003-3071-8358
Brian Fleming https://orcid.org/0000-0002-2129-0292
Nicholas Nell https://orcid.org/0000-0001-7131-7978
Ambily Suresh https://orcid.org/0000-0002-0506-0825
P. Wilson Cauley https://orcid.org/0000-0001-9207-0564
Jean-Michel Desert https://orcid.org/0000-0002-0875-8401
Pascal Petit https://orcid.org/0000-0001-7624-9222
Aline A. Vidotto https://orcid.org/0000-0001-5371-2675

References

Bello-Arufe, A., Buchhave, L. A., Mendonça, J. M., et al. 2022, A&A, 662, A51
Borsa, F., Fossati, L., Koskinen, T., Young, M. E., & Shulyak, D. 2021, NatAs, 6, 226
Borsa, F., Rainer, M., Bonomo, A. S., et al. 2019, A&A, 631, A34
Borsato, N. W., Hoeijmakers, H. J., Cont, D., et al. 2023a, A&A, 683, A98
Borsato, N. W., Hoeijmakers, H. J., Prinoth, B., et al. 2023b, A&A, 673, A158
Cauley, P. W., Shkolnik, E. L., Ilyin, I., et al. 2019, AJ, 157, 69
Cubillos, P. E., Fossati, L., Koskinen, T., et al. 2024, A&A, 683, A98
Cubillos, P. E., Fossati, L., Koskinen, T., et al. 2020, AJ, 159, 111
Egan, A., Nell, N., Suresh, A., et al. 2023, AJ, 165, 64
Egan, A., France, K., Fleming, B. T., et al. 2020, Proc. SPIE, 11444, 1144406
Eggleton, P. P. 1983, ApJ, 268, 368
Espinoza, N., & Jordán, A. 2015, MNRAS, 450, 1879
Fleming, B. T., France, K. C., Nell, N., et al. 2018, JATIS, 4, 014004
Fossati, L., Biassoni, F., Cappello, G. M., et al. 2023, A&A, 676, A99
Fossati, L., Haswell, C. A., Froning, C. S., et al. 2010, ApJL, 714, L222
Fossati, L., Young, M. E., Shulyak, D., et al. 2021, A&A, 653, A52
France, K., Fleming, B., Egan, A., et al. 2023, AJ, 165, 63
García Muñoz, A., & Schneider, P. C. 2019, ApJL, 884, L43
Gaudi, B. S., Stassun, K. G., Collins, K. A., et al. 2017, Natur, 546, 514
Gressier, A., Lecavelier des Etangs, A., Sing, D. K., et al. 2023, A&A, 672, A34
Haswell, C. A., Fossati, L., Ayres, T., et al. 2012, ApJ, 760, 79
Hoeijmakers, H. J., Ehrenreich, D., Heng, K., et al. 2018, Natur, 560, 453
Hoeijmakers, H. J., Ehrenreich, D., Kitzmann, D., et al. 2019, A&A, 627, A165

Huang, C., Arras, P., Christie, D., & Li, Z.-Y. 2017, ApJ, 851, 150
Huang, C., Koskinen, T., Lavvas, P., & Fossati, L. 2023, ApJ, 951, 123
Ivshina, E. S., & Winn, J. N. 2022, ApJS, 259, 62
Jones, K., Morris, B. M., Demory, B. O., et al. 2022, A&A, 666, A118
Kama, M., Folsom, C. P., Jermyn, A. S., & Teske, J. K. 2023, MNRAS, 518, 3116
Kitzmann, D., Heng, K., Rimmer, P. B., et al. 2018, ApJ, 863, 183
Kreidberg, L. 2015, PASP, 127, 1161
Lothringer, J. D., Barman, T., & Koskinen, T. 2018, ApJ, 866, 27
Lothringer, J. D., Sing, D., Rustamkulov, Z., et al. 2022, Natur, 604, 49
Lowson, N., Zhou, G., Wright, D. J., et al. 2023, AJ, 165, 101
Medallon, S., Rickman, E., & Brown, J. 2023, STIS Instrument Handbook for Cycle 32, Vol. 23 (Baltimore, MD: STScI), 23
Nell, N., DeCicco, N., Ulrich, S., France, K., & Fleming, B. 2021, Proc. SPIE, 11821, 1182117
Newville, M., Stensitzki, T., Allen, D. B., & Ingargiola, A. 2015, LMFIT: Nonlinear Least-square Minimization and Curve-fitting for Python, v0.8.0, Zenodo, doi:10.5281/zenodo.11813
Pedregosa, F., Varoquaux, G., Gramfort, A., et al. 2011, JMLR, 12, 2825
Sing, D. K., Lavvas, P., Ballester, G. E., et al. 2019, AJ, 158, 91
Sreejith, A. G., Fossati, L., Ambily, S., et al. 2022, PASP, 134, 114506
Sreejith, A. G., France, K., Fossati, L., et al. 2023, ApJL, 954, L23
Turner, J. D., de Mooij, E. J. W., Jayawardhana, R., et al. 2020, ApJL, 888, L13
van Dokkum, P. G. 2001, PASP, 113, 1420
Wakeford, H. R., Sing, D. K., Evans, T., Deming, D., & Mandell, A. 2016, ApJ, 819, 10
Wakeford, H. R., Sing, D. K., Stevenson, K. B., et al. 2020, AJ, 159, 204
Wong, I., Shporer, A., Kitzmann, D., et al. 2020, AJ, 160, 88
Yan, F., & Henning, T. 2018, NatAs, 2, 714
Yan, F., Casasayas-Barris, N., Molaverdikhani, K., et al. 2019, A&A, 632, A69